MEASURING EVAPOTRANSPIRATION AND VIRTUAL POTENTIAL HEAT FLUX USING LIDAR

FINAL REPORT

by

W. Eichinger, J. Nichols, D. Cooper, L. Hipps, H. Holder,
C. Neale, and J. Prueger

Sponsored by

NASA

IIHR Technical Report No 458

IIHR - Hydroscience & Engineering
College of Engineering
University of Iowa
Iowa City, IA 52242-1585

October 2006

TABLE OF CONTENTS

LIST OF TABLES

LIST OF FIGURES

MEASURING EVAPOTRANSPIRATION AND VIRTUAL POTENTIAL HEAT FLUX USING LIDAR

Final Report

by

W. Eichinger[1], J. Nichols[1], D. Cooper[2], L. Hipps[3], H. Holder[4], C. Neale[3], and J. Prueger[5]

I. BACKGROUND

The Soil Moisture - Atmosphere Coupling Experiment(SMACEX) was designed to provide a multiscale dataset of vegetation, soil, and atmospheric states, representing a mixture of point, linear, and gridded coverage (Kustas et al., 2006). The SMACEX campaign was conducted simultaneously with the Soil Moisture Experiment 2002 (SMEX02), whose primary objectives were to extend microwave soil moisture observations and retrieval algorithms to rapidly changing crop biomass conditions, to acquire data required to validate the Earth Observing System (EOS) Aqua Advanced Microwave Scanning Radiometer (AMSR)-E brightness temperatures and soil moisture retrieval algorithms, and to evaluate new soil moisture sensing instruments (Njoku et al. 2004). The soil moisture maps that will be generated from the various sensors will provide a key boundary condition for land surface modeling.

The data from SMACEX and SMEX02 was intended be used to address several scientific research topics/issues related to land surface–atmosphere dynamics. These include:

1.) the evaluation of spatial scaling techniques and assumptions inherent in turbulent transport modeling,

2.) the direct evaluation of the role of the spatial and temporal variability in soil moisture and vegetation conditions on soil–vegetation–atmosphere interactions and on local- and regional-scale fluxes, and

3.) the exploration of opportunities for assimilating remote sensing products in order to improve land surface process modeling.

Results of this research will lead to a greater understanding of the role of soil moisture and vegetation conditions on pla1netary boundary layer dynamics for this

[1] IIHR - Hydroscience & Engineering, University of Iowa, Iowa City, IA
[2] Los Alamos National Laboratories, Los Alamos, NM
[3] Utah State University, Logan, UT
[4] Duke University, Durham, NC
[5] USDA Soil Tilth Laboratory, Ames, IA

region, and an assessment of the utility of remote sensing data for improving coupled land–atmosphere models. This, in turn, will lead to more reliable weather forecasting and regional climate predictions. More specifically, the data and research results will assist in substantiating a growing body of evidence from model simulations that suggest that agricultural practices can modify the local and regional climate (Adegoke et al. 2003; Weaver and Avissar 2001). More immediate impacts from the SMACEX project will come from research results evaluating the significance of soil moisture/soil texture differences, phenological differences between the two main agricultural crops, and differences in management practices (i.e., conventional till, no till, ridge till, row spacing) on the land surface energy exchanges across this landscape. Moreover, as a result of the partial canopy coverage during crop development and varying crop and tillage practices, which includes row spacing and orientation, crop cover is not uniform. Consequently, the interpretation of remotely sensed data (including thermalinfrared data and vegetation indexes), and the subsequent estimation of soil and vegetation energy exchanges, will be affected. The significance of these effects on land surface model output at the canopy, field, and regional scales will be addressed with the SMACEX dataset.

II. SITE DESCRIPTION

Site description The SMACEX study site, a grid box 10 km north-south by 30 km east–west, encompassed the Walnut Creek (WC) watershed (centered at 41.96°N, 93.6°W), which has been intensively monitored by the U.S. Department of Agriculture (USDA) Agricultural Research Service (ARS) National Soil Tilth Laboratory (NSTL) since 1990 as a field/watershed study site (Hatfield et al. 1999b). This WC experimental domain was nested within a regional (Iowa, hereafter IA) study area (95 km north–south 40 km east–west) that is used by SMEX02 to encompass several AMSR-E pixels.

The land cover in the WC study area is primarily comprised of corn- (Zea mays L.) and soybean [Glycine max (L.) Merr.] fields. A land use map generated for the site indicates that nearly 95% of the region is in corn and soybean production, with the remaining land cover being comprised of cereal crops, urban areas/roads/farmsteads, forested/riparian areas, and lakes/rivers. The typical field size is on the order of 25 ha, but ranges from 1 to 130 ha. Although the WC watershed covers a relatively small area (5100 ha), it contains all land cover types representing WC and IA experimental domains. In fact, even the WC and IA experimental domains are relatively small compared to the regional climate scale, however, both have topography and soil that are representative of the Des Moines lobe, which covers approximately 1/4 of the state of Iowa (Hatfield et al.

1999b). Moreover, the corn and soybean production in this part of the state is indicative of a much larger agricultural region, namely, the upper Midwest corn–soybean region of the United States, which comprises over 60 million ha and represents 60% of all U.S. cultivated cropland.

The climate in this region is humid, with an average annual rainfall of 835 mm. In a typical growing season, the most rapid growth in corn and soybean crops is observed in the months of June and July, with corn biomass reaching 3–4 kg m^{-2}, while there can be a soybean biomass of 1–2 kg m^{-2}. This translates to leaf area index (LAI) values (by definition, one sided) for corn on the order of four and two for soybean, with both crops completely covering the soil surface. Rainfall events in the spring and summer are often thunderstorms, providing brief and intense showers (Hatfield et al. 1999a). A rain gauge network in and around the watershed monitored by NSTL indicates that the heaviest precipitation months are May and June (about 1/3 of the annual total). The topography is characterized by low relief and poor surface drainage.

Nearly 75% of the watershed is essentially flat, except for the "prairie potholes," while the remaining 25% contains more topographic relief and more dissected streams, and has better drainage. The soils are clay and silty clay loams, with generally low permeability (Hatfield et al. 1999b). A soils map for the WC region indicates that sandier soils are located near tributaries and in the eastern end, but in most other areas the soil texture is fairly uniform. Anthropogenic forces have significantly modified the hydrologic character of the basin over the past 100 years.

III. EXPERIMENTAL DESIGN

The intensive measurement campaign for SMACEX mainly covered the period from 15 June [day of year (DOY) 166] through 8 July (DOY 189). During this period, remote sensing data were collected from ground, aircraft, and satellite platforms. The SMEX02 campaign started later, on 25 June (DOY 176), and ended on 12 July (DOY 193). During the overlap of the two field campaigns, the vegetation grew rapidly and surface soil moisture changed from dry to wet from rainfall events in early July.

The WC study area was the focus of SMACEX measurement activities, as well as extensive vegetation and soil moisture sampling for SMEX02 of the over 30 field sites. A major part of SMACEX involved measurements of surface energy, water, and carbon fluxes, as well as mean and turbulent atmospheric boundary layer (ABL) properties, and the collection of very high resolution visible, near-infrared, and thermal-infrared remote sensing imagery. The measurements are briefly described below, with more detailed

information provided in the next section. In Appendix 1, a summary of the frequency and duration of measurements in support of SMACEX is provided.


Figure 1. The UI lidar setup in the cornfield.

Central to the SMACEX measurement activities was the deployment of meteorological - flux (METFLUX) towers employing eddy covariance (EC) at 12 field sites (6 corn and 6 soybean) distributed throughout the WC study area. The towers were instrumented with sensors for measuring turbulent fluxes of water vapor and sensible heat, as well as net radiation and soil heat flux, with a subset measuring carbon dioxide flux. Additional hydrometeorological observations included wind speed and direction, air temperature, vapor pressure, near-surface soil temperature and moisture, and below and above-canopy radiometric surface temperature. At one site, three ground-based light detection and ranging (lidar) systems from the Los Alamos National Laboratory (LANL) and the University of Iowa (UI), measuring ABL water vapor, height, and cloud cover and properties, was placed at the boundary between a corn and soybean field (Fig. 1). Atmospheric radiosoundings and acoustic sonic detection and ranging (sodar) soundings were also collected at this location, providing ABL profiles of wind speed and direction, virtual temperature, and humidity.

IV. EDUCATIONAL AND OUTREACH ACTIVITIES

We have involved four undergraduate students in the field experiments and the data analysis. This is beneficial to them in that they gain field experience. The students also participated in the data analysis which was presented at several mini-conferences at UI. An additional student is involved that is a visiting graduate researcher from Poland.

The data collected is used in the graduate level Hydrometeorology course at UI (53:178). The students used the data with a simple surface-atmosphere model to explore the effects of changes in the surface properties as part of an extended homework assignment.

V. RESULTS

A. Raman Lidar Evapotranspiration Estimates. Raman lidars use a technique

originally pioneered by Fiocco and Smullins (1963), Cooney *et al*. (1969), Cooney (1970), and Melfi *et al*. (1969). A Raman lidar operates by emitting a pulsed laser beam, usually in the ultraviolet or near ultraviolet, into the atmosphere. Atmospheric gases, such as nitrogen, oxygen, and water vapor interact with this light via the Raman scattering process, causing light of longer wavelengths to be scattered. The amount of the wavelength shift is unique to each molecule. This enables the measurement of different atmospheric gaseous species by this technique.

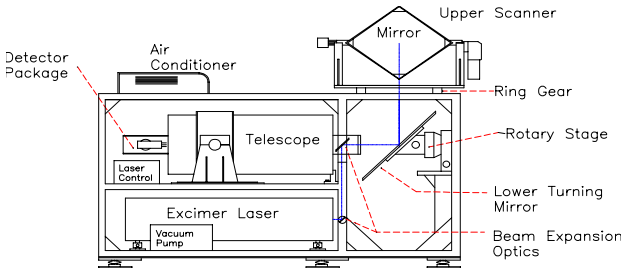

Figure 2. Diagram showing the layout of the Los Alamos Raman lidar. With the exception of the scanning mirror, the arrangement is typical of Raman lidars.

The University of Iowa / Los Alamos National Laboratory (LANL) Raman lidar (shown schematically in Fig. 2) is a typical Raman lidar. In this lidar, the laser is mounted below the telescope. A series of mirrors and lenses is used to expand the beam to make it eyesafe and collinear with the telescope. A forty-five-degree angled mirror is used to change the optical direction to vertical allowing the system to make vertical soundings. With the scanning mirror mounted, the system can perform three dimensional scanning near the earth's surface. At the back of the telescope, a series of dichroic beam splitters are used to separate the elastically scattered light from the light at the two Raman shifted wavelengths from nitrogen and water vapor. Narrow band interference filters block unwanted wavelengths in each channel. To work during the day, many systems operate in the region of the spectrum below about 300 nm where ozone and oxygen strongly absorb sunlight and are thus "blind" to solar photons. Solar blind operation requires the use of a laser near 250-260 nm so that the Raman shifted lines will be below 300 nm. Because of the limited amount of returning light, Raman lidar systems tend to use large, powerful lasers and large telescopes. Therefore, they are unusually large and require significant amounts of power. The typical maximum horizontal range for the LANL lidar is approximately 700 m when scanning, with a corresponding spatial resolution of 1.5 m over that distance. The upper scanning mirror allows three dimensional scanning in 360 degrees in azimuth and ±22 degrees in elevation.

The Raman technique obtains the water vapor mixing ratio, $q_w(r)$, from the ratio of the signal magnitude in the water vapor channel, $P_{H2O}(r)$ to the magnitude of the signal in the nitrogen channel, $P_{N2}(r)$, using (Melfi, 1972):

$$q_w(r) = \frac{P_{H2O}(r)}{P_{N2}(r)} \left[\frac{C_{N2}\ \sigma_{N2}\ M_{N2}}{C_{H2O}\ \sigma_{H2O}\ M_{H2O}\ fr_{N2}} \right] \exp\left[\int_0^h [\kappa_t(r', \lambda_{N2,R}) - \kappa_t(r', \lambda_{H2O,R})] dr' \right] \quad (1)$$

where $\lambda_{N2,R}$ and $\lambda_{H2O,R}$ are the Raman N_2 and H_20 scattered wavelengths; $P_{N2}(r)$ *and* $P_{H2O}(r)$ are the received signals in the nitrogen and water vapor channels; σ_{N2} and σ_{H2O} are the Raman backscatter cross-sections for the laser wavelength; $n_{N2}(r)$ and $n_{H2O}(r)$ are the number density of nitrogen and water molecules at range, r; $\kappa_t(r, \lambda_{N2,R})$, and $\kappa_t(r, \lambda_{H2O,R})$ are the total attenuation coefficients at the Raman-shifted wavelengths of nitrogen and water vapor molecules; fr_{N2} is the fractional N_2 content of the atmosphere (0.78084); and C_{N2} and C_{H2O} are the system coefficients which take into account the effective area of the telescope, the transmission efficiency of the optical train, and the detector quantum efficiency at the Raman shifted wavelengths. Thus the water vapor mixing ratio at any distance is given by the ratio of the magnitude of the signal in the water vapor channel to the magnitude of the signal in the nitrogen channel, a multiplicative constant (the part in square brackets in Eq. 1), and a small exponential correction due to difference in extinction between the nitrogen-shifted and water vapor shifted wavelengths. Comparison of the lidar signals to conventional hygrometers can be used to determine the multiplicative constant. Because the signal to noise ratio decreases with distance, the uncertainty in the mixing ratio values is a function of distance from the lidar. For a mid-range distance (~350 m), the estimated uncertainty is approximately 3.6 percent. This is consistent with the comparisons of lidar and calibrated references over land surfaces along horizontal paths. The standard deviation between the lidar and capacitance hygrometer data taken at concurrent times and locations was found by regression to be ±0.34 g/kg (Eichinger *et al*., 2000; Cooper *et al*., 1996).

When the Raman lidar aims along a given line of sight, data are obtained every 1.5 m along that line. By aiming the lidar in a series of different directions, a two or three dimensional map of the water vapor concentrations can be assembled. Figure 3 is a typical scan from the LANL Raman lidar showing the water vapor concentration

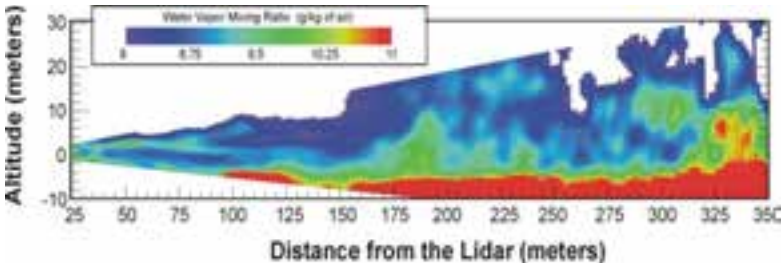

Figure 3. A vertical scan showing the water vapor concentration in a vertical plane above the corn canopy during SMEX02. The day is strongly convective. Red colors represent areas of high water vapor concentration, while blue colors represent lower concentrations. The intense red color at the bottom is a result of the attenuation of the laser beam by the ground or canopy (in this case, corn). The change in the lidar signal as it reaches the canopy top enables one to determine the shape and orientation of the surface.

in one vertical plane in a cornfield in Iowa during the Soil Moisture - Atmospheric Coupling Experiment (SMACEX). The intense red color at the bottom is a result of the attenuation of the laser beam by the ground or canopy (in this case, corn). The change in the lidar signal as it reaches the canopy top enables one to determine the shape and orientation of the surface.

B. Latent Heat Fluxes from Raman Lidar. The water vapor concentration in the vertical direction can be described using the Monin-Obukov Similarity Method (MOM) (Brutsaert, 1982). With this theory, the relationship between the water vapor concentration at the surface and that at some height, *z*, within the inner region of the boundary layer is:

$$q_s - q(z) = \frac{E}{L_e k u_* \rho}\left[\ln\left(\frac{z-d_0}{z_{ov}}\right) - \psi_v\left(\frac{z}{L}\right)\right] \quad (2)$$

where the Monin-Obukhov length, *L*, is defined as:

$$L = -\frac{\rho u_*^3}{kg\left[\frac{H}{Tc_p}+0.61E\right]} \quad (3)$$

z_{0v} is the roughness length for water vapor, q_s is the surface specific humidity, *T*, is the atmospheric temperature, *q(z)* is the specific humidity at height *z*, *H* is the sensible heat flux, *E* is the latent energy flux (the evapotranspiration rate), ρ is the density of the air, L_e is the latent heat of evaporation for water, u_* is the friction velocity (Brutsaert, 1982), *k* is the von Karman constant, taken as 0.40, d_0 is the displacement height, and *g* is the acceleration due to gravity. Ψ_v is the Monin-Obukhov stability correction function for water vapor and is calculated for unstable conditions as:

$$\psi_v\left(\frac{z}{L}\right) = 2\ln\left[\frac{(1+x^2)}{(1+x_{ov}^2)}\right]$$

where :

$$x = \left(1 - 16\frac{z}{L}\right)^{1/4}$$

and where x_{ov} represents the function x calculated for the value of z_{ov}. The roughness length is a site-specific free parameter that can be calculated from the lidar data. The Monin Obukhov length, L, is negative when the atmosphere is unstably stratified. This kind of condition occurs when the soil/canopy is warmer than the air above and convective mixing will occur. The value is positive when the atmosphere is stably stratified. In this case, the potential temperature increases with altitude, suppressing vertical transport. L is infinite in a neutral atmosphere, when the potential temperature is constant with altitude. This condition normally occurs only in the transition from day to night or night to day, but may occur when the winds are exceptionally still.

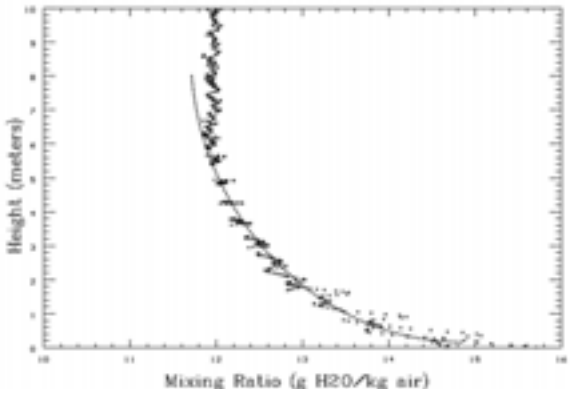

Figure 4. An example of a lidar fitted vertical profile and the data from which it was calculated. The data are a 25 m section from a vertical scan over salt cedar near the Rio Grande River. The variability in the data about the fitted line is due to the presence of discrete structures. If a large enough area is averaged, the mean value at each elevation converges to a logarithmic profile.

Heat and momentum fluxes are often determined from measurements of temperature, humidity, and wind speed at two or more heights. These relations are valid in the inner region of the boundary layer where the atmosphere reacts directly to the surface. This region is limited to an area between the roughness sublayer (the region directly above the surface roughness elements) and extending to a height of five to thirty meters above the canopy top. The concentrations of passive scalars are logarithmic with height in this region. The vertical extent of this layer is highly dependent upon the local conditions and wind velocity. The top of this region can be readily identified by a fairly strong departure from the logarithmic profile found near the surface. Fig. 4 is an example of a water vapor profile with a logarithmic fit showing such a departure at approximately five meters above the canopy top. It has been suggested that the atmosphere is logarithmic to higher levels and may integrate fluxes over large areas (for example, Brutsaert, 1998) so that large scale fluxes could potentially be obtained from profiles high into the boundary

layer.

The flux estimation method as currently used (Eichinger *et al*, 1993; 2000) begins by rearranging Eq. 2 into a linear form:

$$q(z) = -Mz' + c \tag{4}$$

where M is the slope of the fitted function ($M = E/(L_e\, k\, u_* \rho)$), z' is a reduced height parameter ($z' = ln(z-d_o) - \Psi_v((z-d_o)/L)$), and c is a regression constant ($c = M\, ln(z_o) + q_s$). Measurements of the slope are made based upon a least squares fit to several hundred measurements of water vapor concentration. Having determined M from the slope of the fitted line, the flux is then

$$E = L_e\, M\, k\, u_*\, \rho \tag{5}$$

where u_* and L are obtained from local measurements using three dimensional sonic anemometers. Note that the surface roughness length, z_0 can be estimated from the value of c obtained from the fit.

The method is similar to other gradient methods for determining fluxes that are well established (Stull, 1988, Brutsaert, 1982). The lidar method is unique in that it uses a large number of measurements to determine the vertical water vapor gradient. The extension of the method to rough terrain presents issues relating to assumptions of horizontal homogeneity as well as the determination of the canopy top location (with respect to the lidar) and the direction of the normal to the surface.

A key capability of the lidar that is useful in estimating fluxes over complex terrain is the ability to determine the location of the canopy top. The lidar is sited so that it overlooks the experimental site and is thus able to determine the location of the canopy top for all of the canopy types. For the case of mixed terrain and canopy, the lidar is used to find the location of the canopy top in the range interval under investigation. The top of the canopy is found either from the abrupt change in the apparent water concentration or from the abrupt change in the elastic lidar signal which is also recorded along each line of sight. The location of the top of the canopy as a function of distance is determined using multiple lines of sight. A linear least squares fit is made to determine the elevation and slope of the top of the canopy within the range interval under consideration.

For an individual water vapor measurement, the distance from the measured point to the surface along a line perpendicular to the measured slope and elevation is used as the corrected height above the surface. This means that the z direction is taken to be the

direction perpendicular to the canopy top and not the vertical (gravitational) direction. The reasoning is that, near the surface, the flow of air will be parallel to the local surface and that dispersion of the water vapor released from the surface in the direction perpendicular to the mean flow is most important to the estimation of evapotranspiration (Kaimal and Finnegan, 1994).

For an individual scan, all of the measurements within the designated region are used to estimate the slope of the single line described by Eq. 4. Fig. 4 is an example of such a fit to a logarithmic profile. While there is spread in the measurements at each height above the ground, the slope can be determined to an accuracy of a few percent. The spread in the measurements are due to the existence of coherent structures containing high and low water vapor concentrations. These structures can be seen in the two dimensional plot shown in fig. 3.

A measured value of the Monin-Obukov length is used to further adjust for atmospheric stability. However, in practice, the use of this correction results in a small (usually less than 3 %) change in the estimated flux. A distinct limitation of this method is the lack of a u_* measurement for each 25 m region. In the ideal case, we divide the region into surface types and use a measured u_* typical of that region. There is evidence that u* is the parameter most likely to be uniform above a canopy Katul *et al.* (1999).

When using this method to determine fluxes, the maximum height for which water vapor measurements are included must be determined. This corresponds to the height of the change in slope shown in Figure 4. While the largest possible distance over which the measurements are made leads to the greatest accuracy, measurements too close

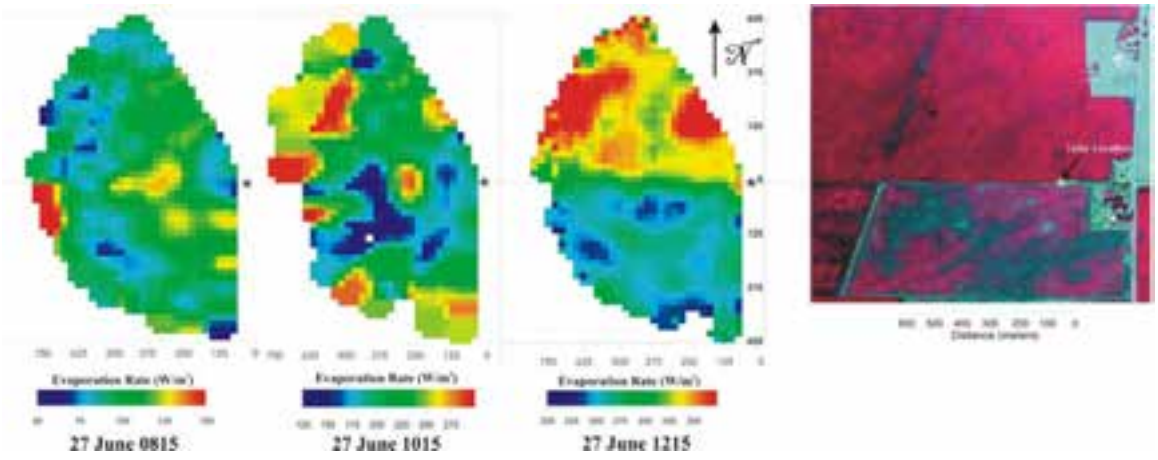

Figure 5. Three evapotranspiration maps of the area around the lidar at various times on June 27th. Red indicates areas of higher evapotranspiration and blues are lowest. In order to show the variability of the fields, the color scales are different for each time. Soybeans were planted to the south of the lidar and corn to the north. The dividing line is the fence that can be seen in the photograph just below the lidar location. Also shown is an aerial three-band false color composite of canopy reflectance (near-infrared (red color), red band (green color) and green band (blue color)) of the site, at the same scale, for comparison. Red colors are indicative of greater amounts of biomass.

to the canopy top (so that they are in the roughness sublayer) or so high that they are outside the inner region lead to erroneous estimates of the water concentration gradient. This height varies throughout the day so the method for determination must be dynamic and adjust to the existing conditions. At present, the maximum and minimum heights for each half-hour averaging period are determined manually by visual inspection of the vertical profiles, a time consuming process.

The evapotranspiration estimate obtained from each of the 25 m squares can be assembled into a map of the evapotranspiration rates over the scanned area. Two examples are presented. Figure 5 has examples of evapotranspiration maps made from 08:15 to 12:15 Central Daylight Time over a corn and soybean fields on June 27th, 2002 during SMEX02. Each map represents a half-hour average (± 15 minutes from the given time). The average height of the corn on June 27th was 1.37 m. The leaf area index was 2.75. The average height of the soybeans on June 27th was 0.30 m. The leaf area index was 1.55. There is also a high-resolution (1.5 meter pixel) multispectral digital image, presented as a false-color composite, of three spectral bands simulating the Landsat Thematic Mapper bands TM2 (green), TM3 (red) and TM4 (near-infrared). The imagery was acquired with the USU airborne multispectral digital system (Neale and Crowther, 1994; Cai and Neale, 1999) on July 1st, at 12:15 CDT. It can be seen that the cornfield canopy (north) had considerably more biomass than the soybean crop (south), which shows distinct patterns of low canopy cover and bare soil. While there are recurring correlations between the deep red areas in the aerial photograph (which are areas of high canopy biomass) and regions of relatively high evapotranspiration rate and conversely, the correlation is not perfect, nor consistent. This is not totally surprising in that the lidar senses the water vapor content in the atmosphere and is thus sensitive to the wind direction and the intermittent nature of turbulence. There is a footprint associated with the lidar measurements. Early in the morning of the 27th, there was sufficient near surface soil moisture so that evapotranspiration was at or near the potential rate. By 10 am, the surface moisture was significantly depleted, but in small local areas, it was possible to have evapotranspiration rates higher than the average. By noon, the evapotranspiration in the soybean area is appreciably lower than that in the corn. Because the leaf area index (LAI) of the soybeans is small (~0.3), it is reasonable to assume that the spatial evapotranspiration rates are dominated by soil moisture considerations.

C. Uncertainty in Evapotranspiration Estimates. The fractional uncertainty of the latent heat flux measurements can be estimated using:

$$\frac{\delta E}{E} = \left[\left(\frac{\delta u_*}{u_*} \right)^2 + \left(\frac{\delta M}{M} \right)^2 + \left(\frac{\delta \rho}{\rho} \right)^2 + \left(\frac{\delta q}{q} \right)^2 \right]^{1/2} \quad (6)$$

where δu_*, δM, , $\delta \rho$, and δq are the uncertainties in the u_*, slope, air density, and water vapor concentration measurements respectively (Bevington and Robinson, 1992). The last term on the right is a contribution from a systematic uncertainty (or bias error) in the lidar measurement of water vapor. While an individual measurement may be uncertain to the three to four percent level (a measure of the precision error), the determination of the mean concentration from a number of measurements (a measure of the bias error) is more accurate. The bias error in the mean value is taken to be less than 2 %. The value of the slope, M, can be estimated with high certainty due to the large number of measurements used in fitting Eq. 4. The nominal uncertainty in the value of the slope is one to two percent. The air density is obtained from local measurements of temperature and air pressure. The uncertainty in the value of the air density is much less than two percent. The value of the friction velocity, u_*, is normally the primary source of uncertainty. While there are no reported estimates of the absolute accuracy of u^* estimates from eddy correlation, it is reasonable to assume that the accuracy will be similar to those for eddy correlation flux measurements which normally range from 5 to 25 percent (Wilson *et al*., 2002). Here, we will assume that the typical uncertainty in u_* is 15 %. The contribution of u_* to the total uncertainty is a function not only of the uncertainty in the measurements of u_* at a given point, but also a contribution from the assumption that a measurement at one point may be applied to a similar surface some distance away (the magnitude of this contribution is highly site specific). For a typical measurement of the evaporative flux, the total uncertainty is determined almost entirely by the uncertainty in u_* and leads us to estimate an overall uncertainty on the order of 15 %. For areas far from u_* measurements, the uncertainty is potentially as much as twice as large. While we use different values of u* for different canopy types, it is assumed that one value of u* is representative for an entire area covered by that canopy. Using a limited number of tower measurements, Katul *et al.* (1999) showed that u* is the parameter most likely to be uniform above a canopy. This lends support for the assumption of that one value can be used over a relatively uniform crop canopy. However, the fractional uncertainty in the evapotranspiration estimate is directly proportional to the fractional uncertainty in u*.

Figure 6 is a comparison of the latent heat flux estimates from eddy correlation measurements with lidar measurements made in the same 25 m region. These measurements represent half-hour averages. The differences between the two instruments are smaller when more data are available from the lidar for either temporal or spatial averaging. The lidar coordinate system is spherical, so that near the lidar, more data are available with which to determine the vertical profile. The smaller the area to be covered, the faster the lidar can revisit the same locations, providing more data for analysis. The calculated values of the latent heat flux were found to be well correlated ($R^2 = 0.84$, with a slope of 0.98) when compared to eddy correlation measurements in the area. The standard error of the flux estimates was 36.5 W/m^2 (14% RMS difference between this method and surface measurements), in keeping with the predicted uncertainty of ~15%.

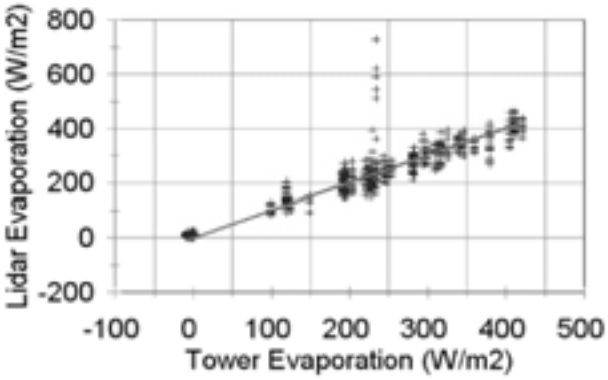

Figure 6. A comparison of eddy correlation evapotranspiration rates over a salt cedar canopy with lidar estimated evapotranspiration rates made in the same 25m lidar pixel. The agreement is generally good and along the 1:1 line. The six point excursion was from an afternoon with exceptionally high winds in which the eddy correlation instruments may have been above the inner region.

D. Effects of Advection. The flux estimation method used assumes that in some region, which is generally taken to be 25 m in size, the slope of the water vapor concentration in the *z* direction can be determined from a curve fit using all of the measurements of the water vapor concentration above that region. This assumes horizontal homogeneity inside the region and with the region immediately upwind, that the aggregate of the values constitutes a measurement of the average condition over the region, and that the slope in water vapor concentration is the result of conditions inside that region. Clearly in transition areas where the canopy type or groundwater availability changes dramatically, these conditions will not apply.

The flux estimation method is not suitable for use near areas with sharp transitions in which moist areas upwind alter the water vapor concentration near the canopy top so that it is not logarithmic with height. When this occurs, the methodology described here cannot be used. When the concentrations are not logarithmic with height, the flux estimation method does not always produce evapotranspiration estimates that are unreasonable and thus this condition can be found only by visual examination of the

vertical scans. In complex terrain, changes in the canopy and elevation lead to changes in the evapotranspiration rate which lead to changes in the water vapor concentration along the surface. The conservation of water vapor equation can be used to estimate the magnitude of the effects.

$$\frac{\partial q}{\partial t} + \bar{u}\frac{\partial q}{\partial x} + \bar{v}\frac{\partial q}{\partial y} + \bar{w}\frac{\partial q}{\partial z} = -\left[\frac{\partial}{\partial x}(u'q') + \frac{\partial}{\partial y}(v'q') + \frac{\partial}{\partial z}(w'q') \right] + \kappa_v \nabla^2 q \qquad (7)$$

Under most circumstances, the diffusion term (the last term on the right), and terms involving $\bar{v}$, $v'q'$, and $\bar{w}$ are small enough to be ignored. Because of advection, changes in evapotranspiration rates may result in flux divergence, particularly in the vertical direction, $\frac{\partial \overline{w'q'}}{\partial z}$. The size of this term can be estimated from the $\bar{u}\frac{\partial \bar{q}}{\partial x}$ and $\frac{\partial \bar{q}}{\partial t}$ terms in the conservation of water vapor equation. It is not uncommon to find horizontal gradients in water vapor concentration on the order of 8 x 10^{-6} kg water/kg air - m between adjacent 25 m by 25 m analysis regions downwind of the riparian area. This can lead to a divergence of about 50 W/m^2 per meter of height above ground. At this time, the effect of advection on the Monin Obukov flux method is unknown, but is a subject of current research. We have found that the corrections due to nonstationarity are, in general, small. The changes in water vapor concentration over a ten minute period are on the order of 3-4 x 10^{-4} kg water/kg air or less. This results in a correction of less than 5 W/m^2.

Related to the question of advection is the question of the location of the source (also known as the footprint) for a measurement at a given height. As noted in the discussion of fig. 6, there is often a systematic offset between the lidar evapotranspiration estimates and likely location of the source. This is a subject of considerable current interest (for example, Leclerc and Thurtell, 1990; Horst and Weil, 1994; Finn et. al, 1996; Horst, 1999). More than two-thirds of the measurements used in any given profile are below 8 m. On more than half of the profiles, the maximum height used is 8 m or less. The greatest curvature in the profile is found at heights less than 4 m, and it is those

measurements from less than 4 m above the canopy that play the greatest role in determining the slope of the line. Using the methodology outlined by Horst and Weil (1994), one can estimate the upwind distance contributing to the flux at a given height. For a height of 8 m and an L value of -20 m, the upwind distance past which less than twenty percent of the flux is generated, is a factor of approximately five to ten times the measurement height, or about 40 to 80 m. This would tend to indicate that the bulk of the flux in a given 25 m section is generated inside that section and the section immediately upwind. Thus it would be prudent to recognize that the flux locations as given by the methodology are not exact, but rather are somewhat diffuse in the upwind direction.

There is also the question of how well the measurements averaged over distances as short as 25 m and less than a minute in time can represent the average conditions. It is noted that in a half-hour estimate, as many as six scans may contribute to the estimate. An individual scan will often show structure near the canopy top. In most cases, this will produce deviations both above and below the average value of the water vapor concentration, but which average to profiles that are logarithmic. Occasionally there are plumes that contain water vapor concentrations that are significantly higher than normal. In such cases, the profiles are significantly altered and may no longer be logarithmic. At present, when such events are found, the evapotranspiration estimate from that 25 m section is discarded. No analysis method has been found which can incorporate such structures to produce an evapotranspiration estimate. A more detailed analysis of the structure of the water vapor concentrations and fluxes is presented in Cooper *et al.*, (2000).

While limitations of the method exist, the amount and type of data provided by the lidar allows one to visually determine what is happening at a particular location that causes the estimates to be anomalous. The existence of visual two dimensional information that allows one to correct for unusual circumstances is a very powerful asset and offers the potential for improved algorithms which may overcome the deficiencies in the current formulation. At present, these conditions require the intervention of a human analyst to determine the proper method of analysis to be made. However, because of the sheer volume of data that must be processed to use this methodology, it must be highly automated if it is to be truly efficacious.

VI. ESTIMATES OF VIRTUAL POTENTIAL HEAT FLUX FROM ELASTIC LIDAR MEASUREMENTS

A. Elastic Lidar Method. Elastic lidars take advantage of the light backscattered from

molecules and aerosols in the atmosphere. Because of the ubiquity of aerosols and the large amount of scattering from them, the magnitude of the return signals are large. This enables small systems with high spatial and temporal resolution. The basic parameters of the transmitter and receiver of the LANL/UI vertically staring lidar system are given in Table 1. The system (Fig. 7 uses a Nd:YAG laser operating at 1.064 microns with a 10 ns laser pulse and a beam divergence of approximately three milliradians. The laser pulse energy is a maximum of 100 mJ with a repetition rate of 50 Hz. The receiver telescope is 25 cm, f/10, commercial Cassegrain telescope. The light is focused to the rear of the telescope where it passes through a 3 nm wide interference filter and two lenses which focus the light onto a 3 mm, IR-enhanced, silicon avalanche photodiode (APD). An iris, located just before the APD serves as a stop to limit the field of view of the telescope.

Figure 7. A photograph of the vertically staring elastic lidar. This system is highly compact and portable and requires no operator input once started.

The laser beam is emitted parallel to the axis of the receiving telescope at a distance of 24 cm from the center of the telescope. There is a minimum distance for which the lidar produces useful data. This is the distance at which the telescope images the entire laser beam, approximately 125 m for this lidar. Only that portion of the lidar signal that comes from the area of complete overlap between the field of view of the telescope and the laser beam can be reliably used for analysis.

A high bandwidth (60 MHz) amplifier is located inside the detector housing. The signal is amplified as part of the detector system and fed to a 100 MHz, 12 bit digitizer on an IBM PC compatible data bus. A computer is used to control the system and to take the data. The computer controls the system using high speed data transfer to various cards mounted on the PC bus. This same multipurpose card is used to both set and measure the high voltage applied to the APD. The digitizers on the PC data bus are set up for data collection by the host computer and start data collection on receipt of the start pulse.

Table 1. Operating Characteristics of the Vertically Staring Lidar System

LANL/UI Vertically Staring Lidar			
Transmitter		**Receiver**	
Wavelength	1064 or 532 nm	Type	Schmidt-Cassegrain
Pulse Length	~ 10 ns	Diameter	0.254 m
Pulse Repetition Rate	50 Hz	Focal Length	2.5 m
Pulse Energy	125 mJ maximum	Filter Bandwidth	3.0 nm
Beam Divergence	~ 3 mrad	Field of View	1.0 to 4.0 mrad adj.
		Range Resolution	1.5, 2.5, 5.0, 7.5 m

B. Virtual Potential Heat Fluxes from Boundary Layer Heights. The height of the boundary layer is a strong function of the heat flux at the surface. The Batchvarova-Gryning model (1991,1994) is based on a one-dimensional approach for the growth of an inversion capped ABL originally developed by Betts (1973), Carson (1973), Tennekes (1973) and Zilitinkevich (1974) (Fig. 8). The Carson and Tennekes model and its more simplified forms have been the basis for nearly all of the boundary layer height models that have been developed. The Batchvarova-Gryning model uses a parameterization of the turbulent kinetic energy budget within the mixed-layer, and of the temperature jump at the mixed-layer top. According to the model, the relationship between the virtual potential heat flux at the surface, $\overline{w'\theta_v'}_{surface}$, the height of the boundary layer, h, and the other surface parameters is:

$$\frac{\overline{w'\theta_v'}_{surface}}{\gamma} = \left[\frac{h^2}{(1+2A)h - 2BkL} + \frac{Cu*^2 T}{\gamma g(1+A)h - BkL}\right]\left[\frac{dh}{dt} - w_s\right] \quad (8)$$

where dh/dt is the growth rate of the boundary layer; t is time; L is the Obukhov length; k is the von Karman constant; g is the acceleration due to gravity; u* is the friction velocity; T is the temperature of the mixed layer; γ is the potential temperature gradient above the boundary layer and w_s is the subsidence velocity. B, and C are normally taken to be parameterization constants with commonly accepted values: B = 2.5, and C = 8 (Melas and Kambezidis, 1992; Gryning and Batchvarova, 1996; Kiillstrand and Smedman, 1997; Steyn *et al*., 1999). A is the ratio of the entrainment of virtual potential heat flux (from the entrainment of warm air above the inversion into the boundary layer) to the surface virtual potential heat flux (Stull, 1988) as:

$$A = -\frac{\overline{w'\theta_v'}_{entrainment}}{\overline{w'\theta_v'}_{surface}} \tag{9}$$

The parameter A can be obtained directly from the lidar data. Knowing that the virtual heat flux is zero near the bottom of the entrainment zone and that the entrainment flux is a maximum at the average height of the boundary layer, and assuming linear changes in the heat fluxes with height (Fig. 8), A can be expressed in terms of the dimensions of the boundary layer (Davies *et al*., 1997). This relationship is written as:

$$A = \frac{h}{h_{bottom}} - 1 = \frac{EZT}{2h - EZT} \tag{10}$$

where h_{bottom} is the height of the bottom of the entrainment zone and EZT is the thickness. There have been many studies that have attempted to measure the entrainment parameter, A. Laboratory experiments and some observational studies have shown the ratio to be approximately A≈ 0.2 for thermally-driven, dry, convective boundary layers (Stull, 1976, 1988; Nicholls and LeMone, 1980). More complicated models that include the mechanical generation of turbulence, or forced convection, (Mahrt and Lenschow, 1976; Zeman and Tennekes, 1977; Smeda, 1979; Driedonks, 1982) and more recent studies (Betts *et al*., 1990, 1992; Culf, 1992; Betts and Ball, 1994, 1995, 1998; Betts and Barr, 1996; Davies *et al*., 1997; Angevine, 1999; Margulis and Entekhabi, 2004) have found values of this entrainment parameter to be significantly larger (A ≈ 0.4) for windy

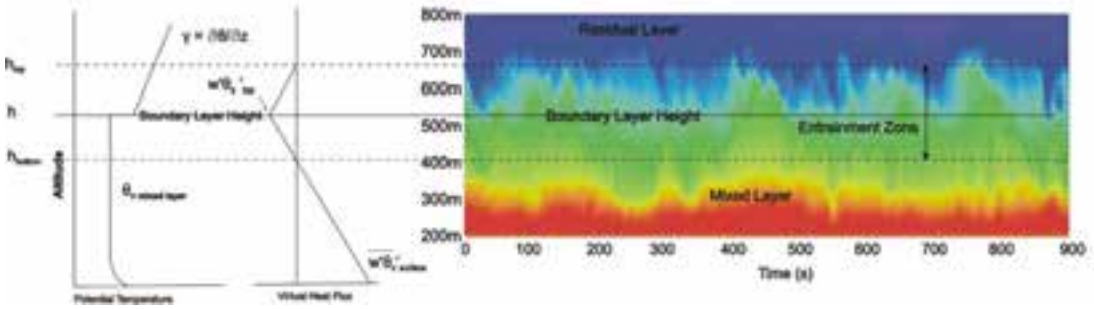

Figure 8. A traditional thermodynamic model of an unstable atmospheric boundary layer. A logarithmic layer near the surface blends into a constant temperature mixed layer that extends to the top of the boundary layer. A stable atmosphere with a temperature inversion acts as a lid to the vertical motions of the air below. A lidar signal showing the height of the boundary layer with time is shown on the right. Reds are highest particulate concentrations and blues are lowest. The thermodynamic diagram is shown to the left scaled to the lidar signal.

conditions. The value of this parameter is dependent on the existing weather conditions. Because of the key role that the entrainment parameter plays, it is fortunate that it can be expressed in terms of the physical size and shape of the top of the boundary layer (Eq. 15), parameters which can be measured directly by the lidar. Figure 9 is a plot of the value of *A* as a function of the potential temperature gradient, γ. Note that the often assumed value $A \approx 0.2$ occurs only for relatively strong gradients.

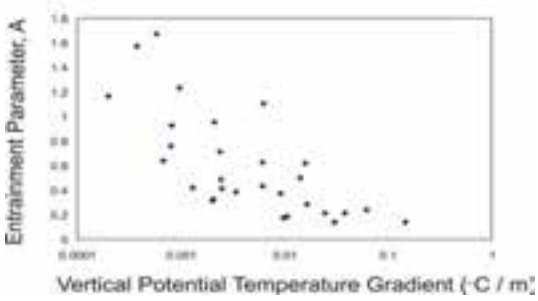

Figure 9. A plot showing the values of A determined for the 25th, 27th, and 29th of June as a function of the potential temperature gradient, γ.

The first term on the right hand side of Eq. (13) represents the growth of the boundary layer due to sensible heat flux from the surface and to the entrainment of warm air from above the boundary layer. The second term is the Zilitinkevich correction which incorporates the contribution to mixed layer growth due to mechanical mixing of the air

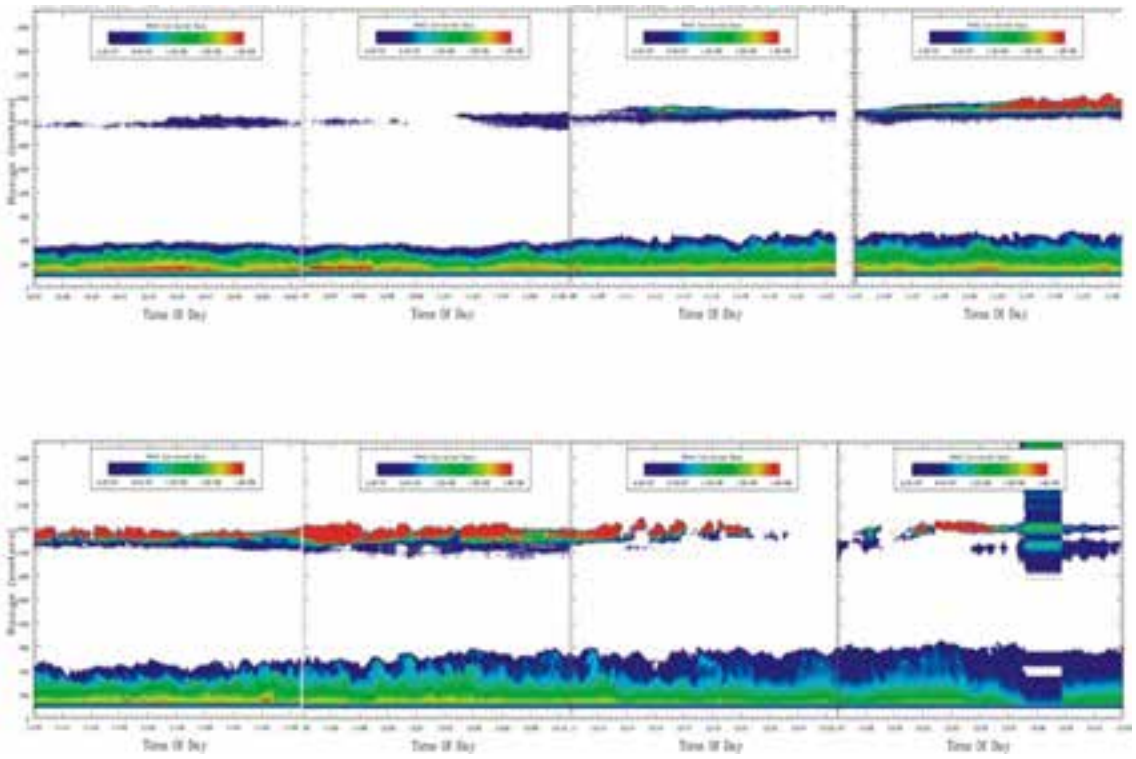

Figure 10. A plot of the lidar data for June 27th from 1040 through 1240. The data is shown as altitude vs time with color showing the relative aerosol content (reds are highest concentrations with blues being the lowest). The blue color above the boundary layer is the residual layer from the previous day. White areas are regions of low aerosol content, generally indicating air from the free troposphere.

near the surface (Zilitinkevich, 1974). Early in the morning when the atmosphere is near neutral and buoyancy is not important, the growth rate of the shallow mixed-layer is proportional to the friction velocity. As the boundary layer grows, buoyancy becomes increasingly important. Mechanical turbulence at the surface ceases to be important when the boundary layer has grown to a height of approximately -1.4L (Gryning and Batchvarova, 1990). Because the lidar, as presently configured, has a minimum altitude of 120m, the only conditions that can be observed are those in which the Zilitinkevich correction is small (less than two percent contribution). Accordingly, the second term has been ignored. Thus, this method is not appropriate for use in the very early morning, when mechanical turbulence is important. The method is useful only during that period when the boundary layer is growing (until approximately the solar noon), since dh/dt is the primary measure used to estimate the energy added to the boundary layer. Once the boundary layer has grown to its maximum height, or has risen to the height of the cumulus cloud bottom, the method cannot be applied.

Given the thermodynamic model in Eq. (13), ignoring the contribution of mechanical turbulence, and assuming a convective boundary layer (L is small), the following equation may be used to relate the virtual potential heat flux to the characteristics of the boundary layer:

$$H_v = \rho c_p \overline{(w'\theta_v')}_{surface} = \rho c_p \left[\frac{dh}{dt} - w_s\right]\left[\frac{\gamma\, h^2}{(1 + 2A)h - 2BkL}\right] \qquad (11)$$

where H_v is the virtual potential heat flux, ρ is the air density, and c_p is the specific heat for air. The last term in parenthesis, when multiplied by ($\rho\, c_p$), represents the amount of energy that must be added to the boundary layer in order for the boundary layer to grow one meter. Thus the rate at which the boundary layer grows is a measure of the rate at which energy is added to the boundary layer. This also implies that for a given temperature profile, there is a one to one relationship between the height of the boundary layer and the total amount of energy that has been added to the boundary layer.

To use Eq. 16, some estimate of the subsidence velocity, w_s, must be found. Vertical motion at the top of the boundary layer is caused by convergence or divergence in the mesoscale flow and is difficult to determine from meteorological measurements. Fortunately, the boundary layer grows into the residual layer from the day before, whose height can be examined to obtain an estimate of the magnitude of the subsidence velocity. Figure 10 contains a plot of a typical lidar return during a convective morning period. The top of the residual layer in this case corresponds to the bottom of the cloud layer at

about 2150 m. For this day, the altitude of the residual layer / bottom of the cloud layer stayed approximately constant until later in the afternoon. . Because the subsidence velocity must be zero at the surface, we assume that the subsidence velocity decreases linearly with height so that:

$$w_s^{height\ \ of\ the\ boundary\ \ layer} = w_s^{top\ of\ the\ residual\ \ layer} \frac{h}{h_{top\ of\ the\ residual\ \ layer}}$$

The height of the residual layer can be found from the same routines used to determine the height of the boundary layer. A review of the various methods that may be used to determine the heights of the boundary layer and entrainment zone and entrainment depth can be found in Kovalev and Eichinger (2004). The residual layer is a region in which the particulate concentration is higher than in the free troposphere above, but less than that in the boundary layer below. In both cases, the routines (discussed below) detect the abrupt drop in particulate concentration that characterizes the boundary between the regions.

The one variable that cannot be obtained in its entirety from lidar data is the Monin Obukhov length, L. To determine L requires values for the air density, ρ, and temperature. The air temperature is easily measured and density can be obtained from local temperature and pressure measurements. The friction velocity, u*, is normally obtained from high speed sonic anemometers that are not normally co-located with lidar systems. This value could be estimated from measurements of the mean wind velocity that could be made from a simple cup anemometer. At worst, if no information is available, constant values for u*, typical of values in the area, could be used (in essence, an educated guess). In such a case, the uncertainty of the estimates of the sensible heat flux would be increased, but since the term containing L is less than 15% of the (1 + 2A)h term, even large errors in u* or L will not have a large effect on the determination of H_v.

C. Uncertainty Analysis. A conventional uncertainty analysis begins with the expression for the virtual potential heat flux expressed in Eq. 16. Standard error propagation methods (Coleman and Steele, 1989; Taylor, 1982) allow estimation of the maximum likely uncertainty of the method as well as indicating those areas that most significantly affect the estimate. Using Eq. 16 to define the heat flux estimate and assuming the measurements are independent, the contributions to the fractional uncertainty in the heat flux from each of the input variables can be found (Table 3).

To estimate the uncertainty, the conditions commonly found at 10:00 am were used as typical input variables (Table 2). The uncertainty estimate for h is, in part, a function of the range resolution of the lidar, which in this case was 2.5m. While the height changes dramatically with time, when averaged over 1800 samples, the likely error is far less than the 5 m estimate made here. For this example, the boundary layer height rose by 97 m in a 30 minute period. The uncertainty in this value is taken to be 5%, which implies the estimate would be in error by 5 m, a value considered to be large. As is seen below, as long as convective conditions exist, the contributions of L to the uncertainty will be relatively small. The fractional uncertainty of a typical value of A of 0.2 is taken to be 10%. Since the manner of estimating this value is still a subject for research, and since A may become as large as 1, the possible uncertainty for this variable may be considered an underestimate. The uncertainty estimate for w_s is made from a 5 m error in estimating the height of the residual layer over a 30 minute period. The value of γ corresponds to a 0.3 degree change in temperature over 53 m. While this value was determined as the slope over that distance, since the data is recorded only to 0.1 degree, the uncertainty could be even higher than the 10% estimate.

Table 2. Typical Conditions used in the Uncertainty Analysis.

Variable	Value	Uncertainty
h	340 m	5 m
dh/dt	0.054 m/s	0.0027 m/s
A	0.2	0.02
L	-30 m	5 m
u*	0.2 m/s	0.04 m/s
γ	0.00567 °/m	0.00057 °/m
w_s	0	0.00278 m/s

Table 3. Contribution to the Fractional Uncertainties from Input Variables

Variable	Fractional Uncertainty Due to Variable
h	$\frac{\delta H}{H} = \frac{(1 + 2A)\,\delta h}{(1 + 2A)h - 2BkL} + \frac{2\,\delta h}{h} = 4.2\%$

dh/dt $$\frac{\delta H}{H} = \frac{\delta\left(\frac{dh}{dt}\right)}{\frac{dh}{dt} - w_s} = 5\%$$

A $$\frac{\delta H}{H} = \frac{2h\,\delta A}{(1 + 2A)h - 2BkL} = 6.25\%$$

L $$\frac{\delta H}{H} = \frac{2Bk\,\delta L}{(1 + 2A)h - 2BkL} = 1.8\%$$

dh/dt $$\frac{\delta H}{H} = \frac{\delta\left(\frac{dh}{dt}\right)}{\frac{dh}{dt} - w_s} = 5\%$$

γ $$\frac{\delta H}{H} = \frac{\delta\gamma}{\gamma} = 10\%$$

w_s $$\frac{\delta H}{H} = \frac{\delta w_s}{\frac{dh}{dt} - w_s} = 5.2\%$$

The total expected fractional uncertainty of 16% is obtained by summing the contributions of the uncertainties in the various measured variables in quadrature:

$$\left(\frac{\delta H}{H}\right)_{total} = \sqrt{\left(\frac{\delta H}{H}\right)^2_{\delta L} + \left(\frac{\delta H}{H}\right)^2_{\delta h} + \left(\frac{\delta H}{H}\right)^2_{\delta A} + \left(\frac{\delta H}{H}\right)^2_{\delta dh/dt} + \left(\frac{\delta H}{H}\right)^2_{\delta w_s} + \left(\frac{\delta H}{H}\right)^2_{\delta\gamma}} \qquad (12)$$

This uncertainty estimate is substantially smaller than a root-mean-square comparison with the eddy correlation instruments (31%) shown in Fig. 11. What is striking about this analysis is that most of the uncertainty comes from the estimate for γ, with the remaining coming from the uncertainties in dh/dt, w_s, and h in that order. Using the variables in Table 2, the contribution to the uncertainty in the heat flux by ignoring the Zilitinkevich correction is less than 1%, but results in a consistent overestimate of H_v.

D. Results. The virtual potential heat fluxes were calculated for morning hours when both lidar and radiosonde data were available for six days during the SMEX experimental period. Virtual heat fluxes were converted to sensible heat fluxes using the method

suggested by Stull (1988). A comparison was made to the average of the two eddy correlation sensors (stations 161 and 162) that were located in the soybean field upwind of the lidar and two eddy correlation sensors (stations 151 and 152) that were located in the corn field downwind of the lidar. While the cornfield was downwind of the lidar, the two fields were typical of the alternating corn/soybean fields found in Iowa. The results are shown in Figure 11. The data agree fairly well with sensible heat flux estimates from eddy correlation instruments in nearby fields. The error bars shown reflect the uncertainty estimate of 16% as calculated above. The calculated values of the sensible heat flux were well correlated with the measured fluxes (R^2 = 0 .79) with a least squares slope of 0.95. However, the standard error of the flux estimates was 21.4 W/m^2, (a root-mean-square difference of 31 percent) a larger value than the predicted uncertainty. The data appears to overestimate the fluxes by a few percent. This suggests that the values for A may be underestimated.

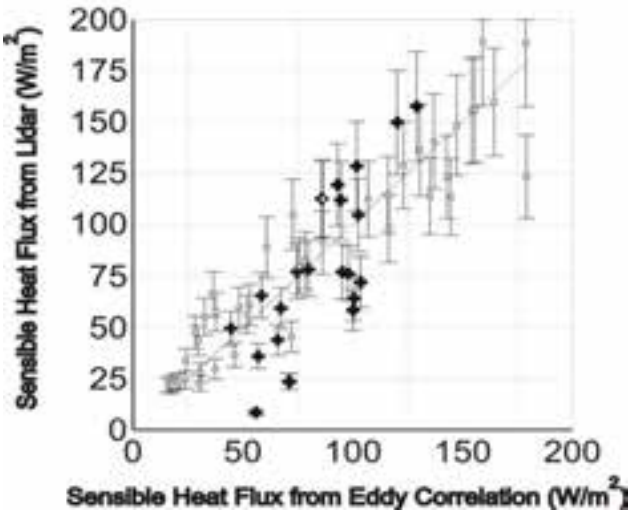

Figure 11. A comparison of virtual potential heat flux estimates from the lidar with virtual potential heat flux estimates from eddy correlation instruments. The data are from five mornings during the SMEX experiment. The crosses are the data for June 27th and correspond to the lidar data shown in Figure 10.

VII. SUMMARY AND FUTURE RESEARCH

Maps of the spatial distribution of evapotranspiration can be produced using spatial water vapor concentration data from a scanning Raman lidar. The estimates of evapotranspiration rates from the lidar compare favorably with other estimates made using the eddy correlation method. The method described allows estimates of the evapotranspiration rate to be made with relatively small (25 m) spatial resolution over an area approaching a square kilometer. Because of the amount of data (25 to 40 Mbytes) and time required to perform the analysis, methods and criteria are currently under development to automate the entire analysis process over all of the azimuthal angles for a given averaging time period. Criteria are being developed to flag and ignore data that do not converge to a logarithmic profile and to not include data above the internal boundary region in the analysis. Automation of the analysis will allow near real time determination

of the evapotranspiration estimates.

While there are significant limitations to the method, it remains a relatively direct method of estimating the fluxes in situations where conventional methods fail or when the topography makes it difficult to site instruments or field enough of them to achieve an areal average. A major limitation is related to changes in the topography, and how much of the atmosphere above a given site can be considered to be influenced by the surface and thus used to estimate the flux in that region. An advantage of this method is that the spatial water vapor measurements themselves can be used to determine the regions in which these problems may occur. The large number of water vapor measurements used to determine the slope also make it possible to determine where the slopes change and thus limit the maximum height of the water vapor measurements used to determine the slope.

Efforts are currently underway to improve the range of the lidar system by increasing the photon efficiency of the system. This will make it possible to scan faster so that more scans can be repeated over a larger area. Efforts are also being made to add the ability to measure spatially resolved temperature using a Raman technique (Nedeljkovic, *et al*., 1993). The addition of temperature will allow determination of the partitioning of solar energy between sensible and latent heat fluxes using similar methods. The ability to estimate these fluxes in a spatial manner will enable progress in a number of fields which examine the role that the canopy plays in partitioning solar energy. Improvements to the inversion algorithms are being made so that auxiliary measurements are not required and which will eliminate issues relating to advection. The ideal inversion method would not require assumptions of homogeneity, would correctly identify the fluxes and the source locations, and not require external meteorological measurements. Therefore, methods of inverting the advection-diffusion equations, Eq 7, to obtain spatially resolved evaporation rates directly are being investigated.

The method used here can provide reliable estimates of the evapotranspiration rate over a relatively large area with relatively fine spatial resolution. The method is a more direct method of estimating the fluxes than most remote sensing techniques that estimate the evapotranspiration rate as a residual. It is however limited in that it assumes a single measurement of the friction velocity is representative of the value over a large region. It also provides regular estimates throughout the day as opposed to intermittent satellite or aircraft measurements. This information can be used in a wide variety of ways to study the spatial variations in evapotranspiration caused by changes in soil type and moisture content, canopy type and topography. Because of the extensive nature of the estimates in space and time, evaluation of the relative contributions of each of these

can be determined. The type of measurements provided also provide the opportunity to span the scales between the footprint of point measurements and the kilometer scale measurements made by satellites.

A method has been presented to estimate the regional virtual potential heat flux from vertically-staring, elastic lidar measurements using the Batchvarova-Gryning model for energy balance in the boundary layer. To use the method, auxiliary measurements of the potential temperature gradient with height from balloons or radiosondes and surface temperature are required. Three variables are obtained from the lidar data; the average boundary layer height, h, the time rate of change in this height, dh/dt, and the ratio of the downward sensible heat flux at the top of the boundary layer to the surface sensible heat flux, A. All three variables are derived from measurements of instantaneous boundary layer heights (here approximately one second apart) over some averaging period.

Comparisons of the sensible heat fluxes from the lidar with eddy correlation measurements are favorable, but with larger errors than expected. A portion of this discrepancy is likely the result of the point nature of the measurements. Both an analysis of the causes of large errors in the estimates and the uncertainty analysis show the importance of accurate measures of γ, the vertical potential temperature gradient. It is important not only to measure the gradient accurately, but also to accurately measure the altitude at which the measured changes occur.

The goal of the effort is to provide information of use to meteorologists and agronomists that is less restrictive than that from conventional point sensors. The use of data from point sensors has required assumptions of heterogeneity in order to be used. It is now increasingly recognized that the world is not uniform, and requires a new world-view that includes the heterogeneity found there.

VIII. REFERENCES

Adegoke, J. O., R. A. Pielke Sr., J. Eastman, R. Mahmood, and K. G. Hubbard, 2003: Impact of irrigation on midsummer surface fluxes and temperature under dry synoptic conditions: A regional atmospheric model study on the U.S. High Plains. *Mon. Wea. Rev.*, **131,** 556–568.

Allen, R.G., M. Tasumi and R. Trezza. 2005. The METRIC Energy Balance and Evapotranspiration Model, ASCE J. Irrigation and Drainage Engineering, in press.

Anderson, M. C., J. M. Norman, G. R. Diak and W. P. Kustas, 1997. A two-source time integrated model for estimating surface fluxes for thermal infrared satellite observations, Rem. Sens. Environ., 60:195-216.

Angevine, W. M.. 1999. Entrainment Results Including Advection and Case Studies from the Flatland Boundary Layer Experiments, J. Geophys. Res., 104:30947–30963.

Bastiaanssen, W. G. M., Menenti, M., Feddes, R. A., and Holtslag, A. A. M. 1998a. A remote sensing surface energy balance algorithm for land (SEBAL): 1. Formulation. J. Hydrol., 198-212.

Bastiaanssen, W. G. M., Pelgrum, H., Wang, J., Ma, Y., Moreno, J., Roerink, G. J., and van der Wal, T. 1998b. A remote sensing surface energy balance algorithm for land (SEBAL): 2. validation, J. Hydrol., 213-229.

Batchvarova, E. and S. Gryning. 1991. Applied model for the growth of the daytime mixed layer. Bound.-Layer Meteor., 56:261–274.

Batchvarova, E. and S. Gryning. 1994. Applied model for the height of the daytime mixed layer and the entrainment zone. Bound.-Layer Meteor., 71:311–323.

Betts, A. K. 1973. Non-Precipitating Cumulus Convection and its Parameterization, Quart. J. Roy. Meteorol. Soc. 99:178–196.

Betts, A. K. and Ball, F. K. 1994. Budget Analysis of FIFE 1987 Sonde Data, J. Geophys. Res. 99:3655–3666.

Betts, A. K. and Ball, F. K. 1995. The FIFE Surface Diurnal Cycle Climate, J. Geophys. Res. 100:25679–25693.

Betts, A. K. and Ball, F. K. 1998. FIFE Surface Climate and Site-Averaged Data Set 1987–1989, J. Atmos. Sci. 55:1091–1108.

Betts, A. K. and Barr, A. G. 1996. First International Satellite Land Surface Climatology Field Experiment 1987 Sonde Budget Revisited, J. Geophys. Res. 101:23285–23288.

Betts, A. K., Desjardins, R. L., and MacPherson, J. I.. 1992. Budget Analysis of the Boundary Layer Grid Flights during FIFE 1987, J. Geophys. Res. 97:18533–18546.

Betts, A. K., Desjardins, R. L., MacPherson, J. I., and Kelly, R. D. 1990. Boundary Layer Heat and Moisture Budgets from FIFE', Boundary-Layer Meteorol. 50:109–137.

Bevington, P, and D. Robinson. 1992. Data Reduction and Error Analysis for the Physical Sciences, McGraw-Hill, Inc, New York, 2nd Ed., 328 pp.

Brutsaert W. 1982. Evaporation Into the Atmosphere, Reidel Pub. Comp., Dordrecht, Holland, 299 pp.

Brutsaert W. 1998. Land-Surface Water Vapor and Sensible Heat Flux: Spatial Variability, Homogeneity, and Measurement, Water Resources. Res., 34:2433-2442.

Cai, B. and C.M.U. Neale. 1999. A method for constructing Three-Dimensional Models From Airborne Digital Imagery". Proceedings of the 17th Biennial Workshop on Color Photography and Videography in Resources Assesment, May 5-7, 1999, Reno, Nevada. American Society of Photogrammetry and Remote Sensing, and Department of Environmental and Resources Sciences, University.

Caparrini, F., F. Catelli, and D. Entekhabi. 2004. Estimation of Surface Turbulent Fluxes through Assimilation of Radiometric Surface Temperature Sequences. J. Hydromet., 5:45-159.

Carson, D.J. 1973. The development of a dry inversion-capped convectively unstable boundary layer. Quart. J. Roy. Meteor. Soc., 99:450–467.

Coleman, H. W. and W.G. Steele. 1989. Experimentation and Uncertainty Analysis for Engineers, John Wiley & Sons, Inc.: New York, NY

Cooney J., J. Orr, and C. Tomasetti. 1969. Measurements Separating the Gaseous and Aerosol Components of Laser Atmospheric Backscatter, Nature., 224:1098-1099.

Cooney J. 1970. Remote measurements of atmospheric water vapor profiles using the Raman component of laser backscatter, J. Appl. Meteoro., 9:182-184.

Cooper, D., W. Eichinger, M. Hynes, C. Keller, C. Lebeda, and D. Poling. 1996. High resolution properties of the equatorial Pacific marine atmospheric boundary layer from lidar and radiosonde observations, J. Atmos. Sci., 53:2054-2075.

Cooper, D.I. W.E. Eichinger, L. Hipps, J. Kao, J. Reisner, S. Smith, S.M. Schaeffer, and D.G. Williams. 2000. Spatial and temporal properties of water vapor and flux over a riparian canopy. Agric. And Forest Meteorol. Special Issue, 105:161-183.

Cooper, D.I., W. E. Eichinger, J. Archuleta, L. Hipps, J. Kao, M. Y. Leclerc, C. M.

Neale and J. Prueger. 2003. Spatial source-area analysis of three-dimensional moisture fields from lidar, eddy covariance, and a footprint model, Ag. For. Met., 114:213-234.

Cooper, D., W. Eichinger, J. Archuleta, L. Hipps, J. Kao, and J. Prueger. 2006. An Advanced Method for Deriving Latent Energy Flux from Lidar Data. Agronomy J. This issue.

Culf, A. D. 1992. An Application of Simple Models to Sahelian Convective Boundary-Layer Growth. Bound. Layer Meteorol. 58:1–18.

Davies, K.J., D.H. Lenschow, S.P. Oncley, C. Kiemle, G. Ehret, A. Giez and J. Mann. 1997. Role of entrainment in surface-atmosphere interaction over the boreal forest. J. Geophy. Res., 102:29219–29230.

Driedonks, A. G. M. 1982. Models and Observations of the Growth of the Atmospheric Boundary Layer, Bound. Lay. Meteor. 23:283–306.

Eichinger, W., D. Cooper, M. Parlange, and G. Katul. 1993. The application of a scanning, water-Raman lidar as a probe of the atmospheric boundary layer, IEEE Trans. on Geosci. and Remote Sensing, 31:70-79.

Eichinger, W., Cooper, D., Forman, P., Griegos, J., Osborne, M., Richter, D., Tellier, L. and Thornton, R. 1999. The Development of a Scanning Raman Water Vapor Lidar For Boundary Layer and Tropospheric Observations. Atmospheric and Oceanic Technology, 16:1753-1766.

Eichinger, W. E., D. I. Cooper, L. C. Chen, L. Hipps, C.-Y. J. Kao and J. Prueger. 2000. Estimation of spatially distributed latent heat flux over complex terrain from a Raman lidar. Agri. And Forest Meteorol.,Special Issue, 105:145-159.

Enting, I.G. 2002. Inverse Problems in Atmospheric Constituent Transport. Cambridge University Press, Cambridge, England.

Finn, D. Lamb, B., Leclerc, M. and Horst, T. 1996. Experimental Evaluation of Analytical and Lagrangian Surface Layer Flux Footprint Models, Boundary Layer Meteorology, 89:283-308.

Fiocco G., and L. D. Smullins. 1963. Detection of Scattering Layers in the Upper Atmosphere (60-140 km) by Optical Radar, Nature, 199:1275-1276.

Gryning, S.E. and E. Batchvarova. 1990. Analytical model for the growth of coastal internal boundary layer during onshore flow. Quart. J. Roy. Meteor. Soc., 116:187-203.

Gryning, S.E. and E. Batchvarova. 1994. Mixed-layer parameterization of the depth of the entrainment zone above the daytime mixed-layer. Quart. J. Roy. Meteor. Soc., 120:47-58.

Gryning, S.E. and E. Batchvarova. 1996. A model for the height of the internal boundary layer over an area with an irregular coastline. Bound. Lay. Met., 78:405-413.

Hatfield, J. L., J. H. Prueger, and D. W. Meek, 1999a: Spatial variation of rainfall over a large watershed in central Iowa. *Theor. Appl. Climatol.*, **64,** 49–60.

Hatfield, J. L., D. B. Jaynes, M. R. Burkart, C. A. Cambardella, T. B. Moorman, J. H. Prueger, and M. A. Smith, 1999b: Water quality in Walnut Creek Watershed: Setting and farming practices. *J. Environ. Qual.*, **28,** 11–24.

Horst, T. and Weil, J. 1994. How Far is Far Enough? The Fetch Requirements for Micrometeorological Measurement of Surface Fluxes, Journal of Atmosperhic and Oceanic Technology, 11:1018-1024.

Horst, T. 1999. The Footprint for Estimation of Atmosphere-Surface Exchange Fluxes by Profile Techniques, Boundary Layer Meteorology, 90:171-188.

Kiillstrand, B., and A.S. Smedman. 1997. A case study of the near-neutral coastal internal boundary layer growth: Aircraft measurements compared with different model estimates. Bound.-Layer Meteor., 85:1-33.

Kaimal, J.C., and Finnigan, J.J. 1994. Atmospheric Boundary Layer Flows, Their Structure and Measurement, Oxford University Press, New York, 289 pp.

Katul, G.G., C.I Hsieh, D. Bowling, K. Clark, N. Shurpali, A. Turnipseed, J. Albertson, K. Tu, D. Hollinger, B. Evans, B. Offerle, D. Anderson, D. Ellsworth, C. Vogel, and R. Oren. 1999. Spatial variability of turbulent fluxes in the roughness sublayer of an even-aged pine forest, Boundary Layer Meteorology, 93:1-28.

Kovalev, V. and W. Eichinger. 2004. Elastic Lidar: Theory, Practice and Analysis Methods, Wiley and Sons, New York.

Kustas,W.P., J.L. Hatfield and J.H. Prueger, 2005, The Soil Moisture–Atmosphere Coupling Experiment (SMACEX): Background, Hydrometeorological Conditions, and Preliminary Findings, J. of Hydromet., 6,pp. 791-804.

Leclerc, M. and Thurtell, G. 1990. Footprint Prediction of Scalar Fluxes using a Markovian Analysis, Boundary Layer Meteorology, 52:247-258.

Mahrt, L. and Lenschow, D. H. 1976. Growth Dynamics of the Convectively Mixed Layer, J. Atmos. Sci. 33:41–51.

Mahrt, L. 1998. Flux Sampling Errors for Aircraft and Towers, Journal of Atmospheric and Oceanic Technology, 15:416-429.

Margulis, S. and D. Entekhabi. 2003. Variational assimilation of radiometric temperature and reference level micrometeorology into a model of the atmospheric boundary layer and land surface, Mon. Wea. Rev., 131:1272-1288.

Margulis, S. and D. Entekhabi. 2004. Boundary layer entrainment estimation through

assimilation of radiosonde and micrometeorological data into a mixed layer model, Bound. Lay. Met., 110:405-433.

Melas, D., and H. Kambezidis. 1992. The depth of the internal boundary layer over an urban area under sea breeze conditions. Bound.-Layer Meteor., 61:247-274.

Melfi S. H., J.D. Lawrence, and M.P. McCormick. 1969. Observation of Raman scattering by water vapor in the atmosphere, Appl. Phys. Lett., 15:295-297.

Melfi S. H. 1972. Remote Measurements of the Atmosphere Using Raman Scattering, Appl. Opt., 11:1605-1611.

Moran, S., R. Jackson, L.H. Raymond, LL.W. Gay, Ph.N. Salter. 1989. Mapping surface energy balance components by combining Landsat Thematic mapper and ground-based meteorological data, Remote Sensing Environ. 30:77-87.

Neale, C.M.U, and B.Crowther. 1994. An airborne multispectral video/radiometer remote sensing system: development and calibration, Remote Sens. Environ. 49:187-194.

Neale, C; Hipps, L.E., Prueger, JH, Kustas, WP, Cooper, DI; Eichinger, W.E. 2001. Spatial mapping of evapotranspiration and energy balance components over riparian vegetation using airborne remote sensing, International Symposium on Remote Sensing and Hydrology 2000; IAHS Pub. no.267:311-315.

Nedeljkovic, D., Hauchecorne, A. and Chanin, M. 1993. Rotational Raman Lidar to Measure the Atmospheric Temperature from the Ground to 30 km, IEEE Transactions on Geoscience and Remote Sensing, 31:90-101.

Nicholls, S. and M.A. LeMone. 1980. The fair weather boundary layer in GATE: The relationship of subcloud fluxes and structure to the distribution and enhancement of cumulus clouds, J. Atmos. Sci. 37:2051-2067.

Njoku, E. G., V. Lakshmi, and P. E. O'Neill, 2004: Preface soil moisture field experiment special issue. *Remote Sens. Environ.,* **92,** 425–426.

Pope, S.B. 1998. Turbulent Flow, Cambridge University Press, Cambridge UK, 771 pp.

Seinfeld, J. and S. Pandis. 1998. Atmospheric Chemistry and Physics, John Wiley & Sons, Inc.: New York, NY

Smeda, M. S. 1979. A Bulk Model for the Atmospheric Planetary Boundary Layer, Bound. Layer Meteorol. 17:411–427.

Steyn, D.G., M. Baldi and R. Hoff. 1999. The detection of mixed layer depth from lidar backscatter profiles. J. Atmos. Oceanic Technol., 16:953–959.

Stull, R. B. 1976. Mixed Layer Depth Model Based on Turbulent Energetics, J. Atmos. Sci. 33:1268–1278.

Stull, R.B. 1988. An Introduction to Boundary-Layer Meteorology, Kluwer Academic

Publishers, Norwell, MA, 666 pp.

Taylor J. R. 1982. An Introduction to Error Analysis, University Science Books.

Tennekes, H. 1973. A model for the dynamics of the inversion above a convective boundary layer. J. Atmos. Sci., 30:558–567.

Weaver, C. P., and R. Avissar, 2001: Atmospheric disturbances caused by human modification of the landscape. *Bull. Amer. Meteor. Soc.*, **82,** 269–281.

Wilson, J.D., G.W. Thurtell, and G.E. Kidd. 1981. Numerical simulation of particle trajectories
in inhomogeneous turbulence, III. Comparison of predictions with experimental data for the atmospheric surface layer. Boundary-Layer Meteorol. 21:443-463.

Wilson, K., A. Goldstein, E. Falge, M. Aubinet, D. Baldocci, P. Berbigier, C. Bernhofer, R. Ceulemans, H. Dolman, C. Field, A. Grelle, A. Ibrom, B. Law, A. Kawalski, T. Meyers, J. Moncrieff, R. Monson, W. Oechel, J. Tenhunen, R. Valentini, and S. Verma. 2002. Energy balance closure at FLUXNET, Ag. and For. Met., 113:223–243.

Zeman, O. and Tennekes, H. 1977. Parameterization of the Turbulent Energy Budget at the Top of the Daytime Atmospheric Boundary Layer, J. Atmos. Sci. 34:111–123.

Zilitinkevich, S.S. 1974. Comments on ‘A Model for the Dynamics of the Inversion above a Convective Boundary Layer.’ J. Atmos. Sci., 32:991–992.

APPENDIX 1: SMEX Data Set

University of Iowa
Data Set

All times are local (DST) except Balloon (GMT) and sodar (CST)

Date	file type	start time	end time	volume #	data quality	notes
14-Jun	NWater	13:06	17:45	69		calibrations
	Mini	9:00	13:18	47		calibrations, gap: 9:22-12:03
	Balloon					none
	Sodar	8:00	17:00			gap 8:30-10:30
15-Jun	NWater	9:40	17:46	69		calibrations
	Mini	10:31	13:41	47		calibrations
	Balloon					1528, 1742, 2028, 2107 GMT
	Sodar	8:15	16:45			
16-Jun	NWater	6:46	17:35	69, 70		
	Balloon					1140, 2022 GMT
	Sodar	5:30	16:45			
17-Jun	NWater	9:58	17:12	71		calibrations
	Mini	9:19	5:24	47		calibrations
	Sounder	10:52	17:18	2	good	calibrations
	Balloon					1427 GMT
	Sodar	8:15	16:45			
18-Jun	NWater	6:46	17:59	71, 72		
	Mini	6:59	18:04	48		
	Sounder	7:24	18:08	2,3	fair	
	Balloon					none
	Sodar	5:30	15:45			
19-Jun	NWater	10:44	13:40	73		calibrations
	Mini	10:51	17:41	48		
	Sounder	10:58	17:17	3	fair	
	Balloon					none
	Sodar	9:45	16:30		poor	
20-Jun	Mini	6:44	18:03	49		
	Sounder	7:06	17:53	3, 4		
	Balloon					none
	Sodar	5:45	17:00			
21-Jun	Mini	6:46	17:59	49		calibrations
	Sounder	7:00	15:02	4	poor	
	Balloon					1817 GMT
	Sodar	5:45	17:15			
22-Jun	Mini	6:53	17:00	49, 50		calibrations
	Sounder	8:25	16:59	5	good	
	Balloon					1745 GMT
	Sodar	6:00	16:00			
23-Jun	NWater	6:45	14:13	73, 74		calibrations
	Mini	6:43	18:19	50		calibrations
	Sounder	6:54	18:18	5, 6	good	calibrations
	Balloon					1752 GMT
	Sodar	5:45	17:30			

24-Jun	Mini	6:33	17:56	50	
	Sounder	6:43	17:10	6	good calibrations
	Balloon				1153, 1458, 1755, 2112 GMT
	Sodar	5:30	17:00		
25-Jun	NWater	14:41	18:03	74	
	Mini	6:39	13:59	51	calibrations
	Sounder	6:56	18:05	6, 7	
	Balloon				1158, 1527, 1811 GMT
	Sodar	5:45	17:00		
26-Jun	NWater	11:06	22:24	75	lidar
	Mini	9:51	22:32	51	calibrations
	Sounder	10:22	22:25	7	good
	Balloon				1502, 1934 GMT
	Sodar	8:45	21:30		
27-Jun	NWater	7:14	17:18	76	lidar
	Mini	7:17	18:16	51, 52	gap: 13:25-17:28
	Sounder	7:35	18:19	7,8	calibrations
	Balloon				1201, 1503, 1913, 2122 GMT
	Sodar	5:30	17:30		
28-Jun	NWater	7:45	18:00	77	calibrations
	Mini	6:46	18:33	52	
	Sounder	6:49	18:35	8	1208, 1602, 1832 GMT
	Balloon				
	Sodar	5:30	17:45		
29-Jun	NWater	7:12	18:00	77, 78	
	Mini	6:58	18:08	53	
	Sounder	6:59	18:21	9	good
	Balloon				1207, 1652, 1917 GMT
	Sodar	6:00	17:00		
30-Jun	NWater	7:04	14:46	78, 79	
	Mini	6:44	15:27	54	
	Sounder	12:55	14:58	9	
	Balloon				1200, 1556, 1834 GMT
	Sodar	5:45	14:15		
1-Jul	NWater	6:59	18:04	79	calibrations
	Mini	6:49	18:16	54, 55	calibrations
	Sounder	8:18	18:14	9,10	calibrations
	Balloon				1202, 1607, 1840 GMT
	Sodar	5:45	17:45		poor
2-Jul	NWater	7:06	17:40	80	
	Mini	6:44	18:02	55	calibrations
	Sounder	6:53	18:39	10	
	Balloon				1158, 1603, 1837 GMT
	Sodar	5:45	15:30		poor
3-Jul	NWater	6:46	11:49	80	
	Mini	6:33	11:48	55	calibrations
	Sounder	6:40	11:42	10	
	Balloon				1148 GMT
	Sodar	10:45	11:45		
6-Jul	NWater	6:55	13:31	80	gap:8:01-13:31
	Mini	6:47	13:42	56	
	Sounder	7:02	13:53	11	gap 8:46-13:35
	Balloon				1216, 1535 GMT

	Sodar	5:45	13:00					
7-Jul	NWater	12:54	14:49	80				
	Mini							
	Sounder	11:06	20:02	11				
	Balloon					none		
	Sodar	10:00	19:30		moderate			
8-Jul	NWater	6:46	11:49	80				
	Mini	7:05	16:58	56		calibrations		
	Sounder	6:57	16:57	11				
	Balloon						1252, 1513, 1853	GMT
	Sodar							
9-Jul	NWater	6:46	11:49	80				
	Mini	7:16	11:16	56		calibrations		
	Sounder	6:52	13:50	11				
	Balloon						1215, 1603, 1836	GMT

APPENDIX 2: SMEX Products

Journal Publications:

Holder, H.L. and W.E. Eichinger, Estimates of the Potential Temperature Profile from Lidar Measurements of Boundary Layer Evolution, accepted by Water Resources Research, 2006.

Eichinger, W.E., D. I. Cooper, L. E. Hipps, W. P. Kustas, C. M. U. Neale, J. H. Prueger, 2005, Spatial and Temporal Variation in Evapotranspiration Using Raman Lidar, Advances in Water Resources, in Press.

W.E. Eichinger and D.I. Cooper, 2006, The Use of Lidar Remote Sensing for Spatially Resolved Measurements of Evaporation and Other Meteorological Parameters, Accepted by Journal of Agronomy.

Eichinger, W.E., H.E. Holder, D.I. Cooper, L.E. Hipps, R. Knight, W. P. Kustas, J. Nichols, and J. H. Prueger, Lidar Measurement of Boundary Layer Evolution to Determine Sensible Heat Fluxes, *Journal of Hydrometeorology*, Volume 6, Issue 6 (December 2005) pp. 840–853.

J. H. Prueger, J. L. Hatfield, W. P. Kustas, L. E. Hipps, J. I. MacPherson, C. M. U. Neale, W. E. Eichinger, D. I. Cooper, and T. B. Parkin , Tower and Aircraft Eddy Covariance Measurements of Water Vapor, Energy, and Carbon Dioxide Fluxes during SMACEX Journal of Hydrometeorology, Volume 6, Issue 6 (December 2005) pp. 954–960.

Conference Proceedings:

L.E. Hipps, J.H. Prueger, W. Eichinger, and W.P. Kustas, Relations Between Environmental Conditions and the Ability to Close the Energy Balance

Eichinger, W E, J. Nichols, D. Cooper, J. Prueger, Observations and modeling of land surface hydrological processes, *Eos Trans. AGU, 86*(48), Fall Meet. Suppl., Abstract H42-06, 2005.

Eichinger, William, and Daniel I. Cooper, The Use of Lidar Remote Sensing for Spatially Resolved Measurements of Evaporation and other Meteorological Variables, ASA Special Symposium on Energy Balance Advances and Measurements, ASA - CSSA - SSSA 49th Annual Meeting, Science to Secure Food and the

Environment, 2004, Seattle WA, 31 Oct-4 November, pg. 176, 2004

Nichols, J., W.E. Eichinger, D.I. Cooper, L.E. Hipps, H.E. Holder, W.P. Kustas, J.H. Prueger, 2004: Lidar Measurement of Boundary Layer Evolution to Determine Sensible Heat Fluxes. *Eos Trans. AGU, 85*(47), Fall Meet. Suppl., Abstract H33E-0509

Eichinger, W E, Cooper, D I, Hipps, L E, Kustas, W P, Neale, C M, Prueger, High Resolution Evaporative Fluxes Over Corn and Soybean Crops from Lidar , J H, *Eos Trans. AGU, 84*(46), Fall Meet. Suppl., Abstract H21H-06, 2003.

Nichols, J J, Eichinger, W E, A Simple Model to Determine the Effects of Surface Inhomogeneity in the Inner Region, *Eos Trans. AGU, 84*(46), Fall Meet. Suppl., Abstract H42A-1059, 2003.

William Eichinger, Daniel I. Cooper, Larry Hipps, John Prueger, and William P. Kustas, Lidar Measurement of Boundary Layer Evolution to Determine Sensible Heat Fluxes, EGS - AGU- EUG Joint Assembly, 2003, Nice, France, 6-11 April, pg. 308, 2003

W. E. Eichinger, D. I. Cooper, L. E. Hipps, W. P. Kustas, C. M. U. Neale, and J. H. Prueger, High Resolution Lidar Evaporative Fluxes Over Corn and Soybean Crops in Central Iowa During SMACEX, 83rd American Meteorological Socieity Conference, Long Beach CA, 9-13 February, 2003.

W. P. Kustas, J. H. Prueger, J.L. Hatfield, J. I. MacPherson, M. Wolde, C. M. U. Neale, W. E. Eichinger, D. I. Cooper, J. M. Norman, and M. C. Anderson, An Overview of The Soil-moisture-atmospheric-coupling-experiment (Smacex) in Central Iowa, 83rd American Meteorological Socieity Conference, Long Beach CA, 9-13 February, 2003.

J. H. Prueger, W. P. Kustas, L. E. Hipps, J.L. Hatfield, A. Cahill, C. Williams, J. I. MacPherson, M. Wolde, J. Albertson, W. E. Eichinger, D. I. Cooper, N. Brunsell,and R. Gillies, Spatial Variability of Turbulent Fluxes Across a Corn /Soybean Production Region in Central Iowa, 83rd American Meteorological Socieity Conference, Long Beach CA, 9-13 February, 2003.